AGU PUBLICATIONS

Radio Science

RESEARCH ARTICLE
10.1002/2015RS005922

Special Section:
URSI AT-RASC (Atlantic Radio Science Conference)

From MAD to SAD: The Italian experience for the low-frequency aperture array of SKA1-LOW

P. Bolli[1], G. Pupillo[2], G. Virone[3], M. Z. Farooqui[3], A. Lingua[4], A. Mattana[2], J. Monari[2], M. Murgia[5], G. Naldi[2], F. Paonessa[3], F. Perini[2], S. Pluchino[2], S. Rusticelli[2], M. Schiaffino[2], F. Schillirò[6], G. Tartarini[7], and A. Tibaldi[3]

[1]INAF, Astrophysical Observatory of Arcetri, Florence, Italy, [2]INAF, Observatory of Radio Astronomy, Bologna, Italy, [3]CNR, Institute of Electronics, Computer and Telecommunication Engineering, Turin, Italy, [4]Polytechnic of Turin, Department of Environment, Land and Infrastructure Engineering, Turin, Italy, [5]INAF, Observatory of Radio Astronomy, Cagliari, Italy, [6]INAF, Catania Astrophysical Observatory, Gravina di Catania, Italy, [7]Department of Electrical, Electronic and Information Engineering, University of Bologna, Bologna, Italy

Key Points:
- Italian demonstrators of low-frequency aperture array for radio astronomy
- Aerial unmanned vehicle for the instrumental calibration of an aperture array
- Technological solutions implemented in the receiving chain of a low-frequency aperture array

Correspondence to:
P. Bolli,
pbolli@arcetri.inaf.it

Citation:
Bolli, P., et al. (2016), From MAD to SAD: The Italian experience for the low-frequency aperture array of SKA1-LOW, *Radio Sci.*, *51*, 160–175, doi:10.1002/2015RS005922.

Received 21 DEC 2015
Accepted 23 FEB 2016
Accepted article online 1 MAR 2016
Published online 15 MAR 2016

Abstract This paper describes two small aperture array demonstrators called Medicina and Sardinia Array Demonstrators (MAD and SAD, respectively). The objectives of these instruments are to acquire experience and test new technologies for a possible application to the low-frequency aperture array of the low-frequency telescope of the Square Kilometer Array phase 1 (SKA1-LOW). The MAD experience was concluded in 2014, and it turned out to be an important test bench for implementing calibration techniques based on an artificial source mounted in an aerial vehicle. SAD is based on 128 dual-polarized Vivaldi antennas and is 1 order of magnitude larger than MAD. The architecture and the station size of SAD, which is along the construction phase, are more similar to those under evaluation for SKA1-LOW, and therefore, SAD is expected to provide useful hints for SKA1-LOW.

1. Introduction

In the last years, the Italian Institute for Astrophysics (INAF) has put significant human and financial resources in the Square Kilometer Array (SKA) project. INAF represents Italy as a Full Member of the SKA Organization and is officially involved in four Consortia responsible for different elements of the SKA telescopes. One of them is the Aperture Array Design and Construction (AADC) Consortium, which works for setting the low-frequency aperture array (LFAA) element of Square Kilometer Array phase 1 (SKA1-LOW) to be built in the Australian desert starting year 2018. Within this Consortium, INAF contributes in the following work packages: the analog receiving system including the RF transportation from the antennas to the central processing station, the antennas/arrays characterization and calibration, and finally the acquisition and digital processing modules both on the hardware and on the firmware sides.

The original idea behind Medicina Array Demonstrator (MAD) and Sardinia Array Demonstrator (SAD) was to have national test benches available to test some innovative components/technologies in a more realistic environment than that provided in the laboratory. In fact, even if MAD and SAD represent small-scale arrays, they assure a complete receiving chain of the whole system from the antennas to the signal processing. Therefore, each new component/algorithm is integrated and tested in a real LFAA system.

MAD is a small project entirely funded by INAF with 75 k€. It was designed and constructed in 2013 and tested in 2014. With the conclusion of MAD, the INAF team started the conceptual design of SAD, which was granted by the Sardinian Regional Government with 300 k€ and by INAF with 120 k€. SAD is currently along the construction phase and is expected to be commissioned in 2016. The size of SAD is such that it will have enough sensitivity and resolution to allow for some basic astronomical tests and demonstrative observations [*Murgia et al.*, 2014].

One critical step toward the final design of the LFAA element of SKA1-LOW is the construction of the verification systems, whose objective is to verify the end-to-end signal path from antenna to the output of the beamformer. In the year 2016, the AADC Consortium will be involved in the construction of the Aperture Array Verification System (AAVS1), which will be the final demonstrator before the construction of SKA1-LOW. The architectures of AAVS1 and SAD are similar, if not identical, in many subelements, for example, the analog receiving chains and the station beam forming. This similarity adds value to the SAD project.

Besides several technological aspects, one of the main issues in the LFAA systems is the instrumental calibration. Due to the physical dimensions of these arrays, the anechoic chamber measurements are not feasible. Therefore, alternative open-air approaches based either on astronomical calibrators or on artificial sources have been considered in the last years [*Chang et al.*, 2015]. Among the latter systems, we developed a radio frequency system mounted on an unmanned aerial vehicle (UAV) consisting of a hexacopter [*Virone et al.,* 2014]. Such a system allows also for the antenna/array experimental characterization. This artificial source was intensively used within MAD for calibrating each antenna to form the array beam in the zenith direction [*Pupillo et al.*, 2015]. As far as SAD is concerned, a numerical analysis has been initiated to evaluate the effects to the calibration due to the mutual coupling among the antennas. A deep understanding of the pros and cons of the application of the artificial source to SAD is particularly relevant and gives useful information on the feasibility of a possible use within SKA1-LOW.

This paper is organized as follows: section 2 describes the technical characteristics of the two demonstrators, whereas section 3 shows the radio frequency environment at the two sites. The aerial system we developed for the instrumental calibration of MAD and SAD is presented in section 4. Several results on the application of this system for calibrating MAD are discussed in section 5, for example, different calibration strategies and the accuracy of the phase patterns measurement. Section 6 shows some preliminary numerical results obtained with a full-wave electromagnetic simulator for SAD, whereas section 7 discusses the lessons learned from MAD and their guidance for SAD and future development. Finally, section 8 reports the conclusions of the work.

2. Technical Description of MAD and SAD

The sites chosen for MAD and SAD are, respectively, the Medicina station, close to Bologna, (latitude 44°31′15″N, longitude 11°38′49″E, altitude 10 m) and the Sardinia Radio Telescope (SRT) site (latitude 39°29′34″N, longitude 09°14′42″E, altitude 600 m) both operated by INAF (see Figure 1).

One of the advantages of the integration of SAD into the SRT observatory is the possibility to exploit existing computing resources. In fact, the SRT site hosts one of the nodes of the high-performance computing infrastructure named Cybersar. Additionally, as the P band receiver (305–410 MHz) installed in SRT partially overlaps the frequency band of SAD (270–420 MHz), possible interesting applications between the two systems can be considered.

MAD was designed to be easily deployed during the measurement tests and to stay in operation for the duration of the experiment in course (usually of the order of 1 week). Therefore, there were no needs to define stringent requirements, especially on the antenna mechanics, for the environmental conditions. Vice versa, SAD is expected to be a permanent demonstrator, lasting for several years, and consequently, it must assure resistance to the environmental parameters present at the SRT site.

The architectures of MAD and SAD are graphically shown in Figure 2. Both are based on a hardware configuration consisting of Vivaldi antennas, radio frequency over fiber (RFoF) links for RF signal transportation, and finally digital data acquisition modules. Table 1 illustrates and compares the main parts of the two demonstrators. As a reference, in the same table, the requirements for the LFAA element of SKA1-LOW and of the verification system AAVS1 have been included.

Although MAD was designed to operate over 16 MHz bandwidth, it was used only for measuring continuous radio frequency waves emitted by artificial sources. Therefore, a 19 kHz channel was stored and processed. The 408 MHz central frequency was chosen to exploit the infrastructures already existing at the Medicina site. On the other hand, SAD is aimed at performing basic astronomical tests, and therefore, a relatively wide bandwidth was chosen. In SAD, the central frequency and the frequency band have been identified taking into account the radio frequency environment measured at the site [*Bolli et al.*, 2015].

The dual-polarized Vivaldi antennas [*Monari et al.*, 2013] for MAD (version 2.0) and for SAD (version 3.1) have been designed to accomplish the SKA requirements (see the baseline design document [*Dewdney*, 2015]). The Vivaldi version 3.1 is composed of a cubic cavity under the four wings (two for each linear polarization), and it adopts a mesh steel structure (whereas the version 2.0 was a solid structure) to reduce its wind resistance. Figure 3 shows some pictures with the general layout of the antennas and a detail of the wings for the electronics integration. Weight and dimensions are 25 kg, $775 \times 775 \times 1125\ mm^3$, and 16 kg, $962 \times 962 \times 1370\ mm^3$, for versions 2.0 and 3.1, respectively.

Figure 1. Geographical positions of MAD and SAD in Italy. The small pictures illustrate the MAD array as built and an artistic view of the SAD array with the Sardinia Radio Telescope in the background.

Differently from SKA1-LOW, the Italian demonstrators do not use a ground plane under the antennas in order to reduce the overall system cost. In this scenario, the noise coming from the ground can intercept the element backlobe producing a nonnegligible contribution to the antenna temperature. This contribution has been evaluated with a full-wave approach. Both the Vivaldi 2.0 and 3.1 have been simulated over a large box of dielectric ($7 \times 7 \times 7$ m) having the complex permittivity of an average soil sample. The computed radiation efficiency η has then been used to estimate the ground noise contribution to the antenna temperature with the formula $T_{ground}^{ant} = T_{ground}^{Phys}(1-\eta)$ [*Kraus*, 1984], where T_{ground}^{Phys} is the physical temperature of the ground (290 K). Figure 4a shows the computed curves for both antennas. As expected, the Vivaldi 3.1 design exhibits a lower T_{ground}^{ant} owing to its reduced backlobe and enanched directivity.

Since a quite large number of antennas were needed for SAD (150 including contingency and possible further tests at the Medicina site), the antenna construction process was optimized to keep the production cost around 300 € per antenna. This constraint also oriented the manufacturing solution toward the wire mesh structure of the Vivaldi 3.1. As a drawback, the thinner mesh structure slightly increases the overall antenna impedance with a consequent increase of the reflection coefficient (see Figure 4b). Nevertheless, the computed values are acceptably below −9 dB in SAD frequency band.

The antenna patterns for both antennas in the frequency range 250–450 MHz are compared in Figure 5. As mentioned above, Vivaldi 3.1 (gray curves on the right) exhibits a higher gain at zenith owing to both the backlobe reduction and the narrower *H* plane (solid lines). Moreover, *H* plane and *E* plane (dashed lines) are closer to each other with respect to the Vivaldi 2.0, providing a better symmetry of the element pattern and a lower Intrinsic Cross-Polarization Ratio (IXR) [*Fiorelli et al.*, 2013] [*Carozzi*, 2015]. The higher gain of the Vivaldi 3.1 leads to a narrower beamwidth, especially at higher frequencies, which in turn provides a reduction of the system sensitivity of about 3 dB for scanning angles larger than 30° from zenith. Although the SKA requirements aim for a larger sky coverage, the obtained performance will not affect the calibration studies that can be performed with SAD. The receiving chains will be calibrated using a flying artificial source having a power level which can be selected according to the available sensitivity levels.

The flexibility in the antenna distribution is one of the more remarkable characteristics of SAD. In fact, the antennas can be moved between different deployment scenarios. This imposed very severe requirements to the antenna version 3.1 mechanics, without fixing the antennas to the ground but supporting them through a heavy movable base (four concrete tiles of 20 kg each).

The two different layouts currently planned for SAD are as follows: 128 antennas distributed over a core of maximum 64 m in diameter or 16 antennas grouped in eight stations of maximum 15 m in diameter each. In this latter configuration, four stations will be inside the core, whereas the other four in satellite stations. The antennas will be randomly spaced in each SAD station. Additionally, they could be oriented either in the same direction or randomly in order to reduce the overall IXR depending on the observation requirement still to be defined. During the excavation and flattening of the areas, it was decided to duplicate the cables infrastructure so either to allow operations for both schemes from the beginning or to double the number of the array elements.

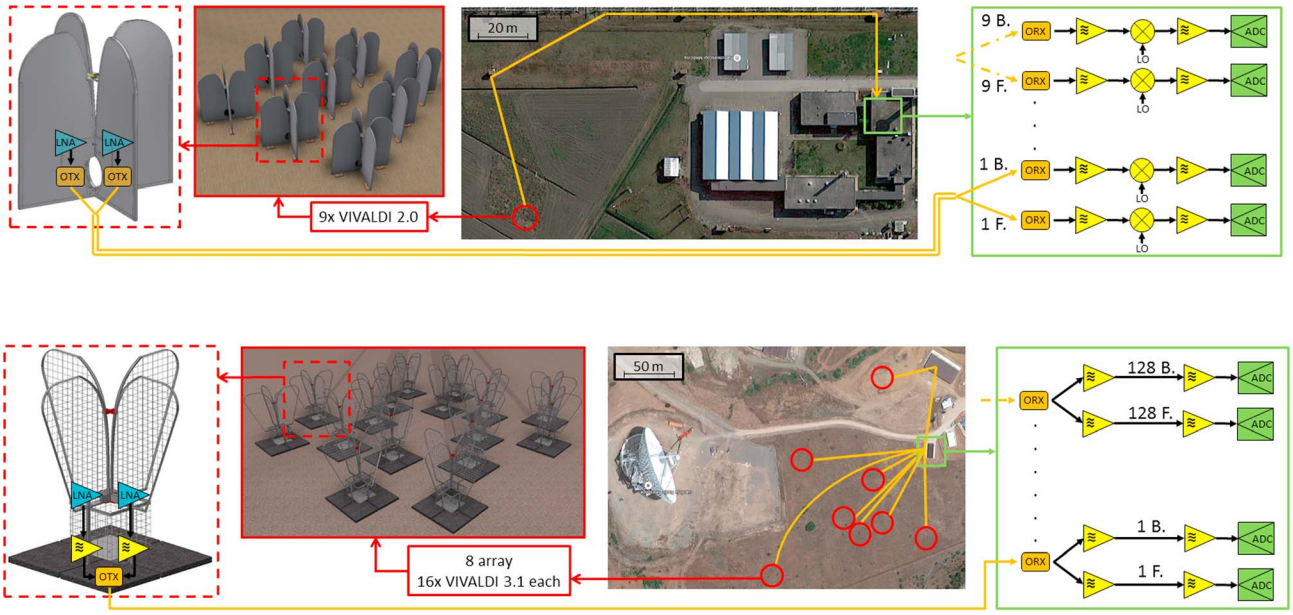

Figure 2. Illustrative schemes of the receiving chain of (top) MAD and (bottom) SAD. Both schemes show the antenna model (with the front end) and the array distribution on the left side, the path of the optical link from the optical transmitter (OTX) to the receiver (ORX) and on the right side the conditioning system between the optical receiver and the analog-to-digital converter. The letters "B" and "F" refer to the two antenna ports: Back and front, respectively.

For both MAD and SAD, each dual-polarized Vivaldi antenna mounts two low-noise amplifiers (LNAs) embedded in the enclosures located in the wings close to the coaxial connectors (Figure 3 (right column)). For both demonstrators, the front ends terminate with an analog RF-to-optical converter for optically transmitting the signal to the data processing center. Additionally, both RFoF links are based on a distributed feedback laser and standard single mode (G652D) optical medium. Differently from MAD, where a conventional solution with independent links has been used [*Perini et al.*, 2009], in SAD, as in AAVS1, an approach based on wavelength division multiplex technique will be exploited. Thanks to this approach, only one fiber is needed to transport both the polarizations of one antenna since the two lasers work at different optical wavelengths. As a consequence, the optical infrastructure (mainly optical fiber cabling and connections) will be halved respect to the standard approach, allowing both cost reduction and better mechanical integration at the receiver level.

The front end of SAD includes an additional radio frequency stage installed below the antenna basement and consisting of a band-pass filter and a second RF gain block. The presence of the second RF gain stage and the use of a preamplified optical transmitter significantly reduce the noise figure of the receiver from 18 dB in MAD to 0.5 dB in SAD.

The MAD antennas were also equipped with batteries for powering the active components of the front end. In SAD, the optical fibers for transmitting the radio frequency are embedded in a hybrid cable containing also the copper pairs for powering the active elements in the antenna. However, SAD will also allow experimentation in the power of fiber (PoF) technology to bring the electrical power to the antennas by means of optical fiber [*Perini et al.*, 2015].

MAD used the analog receiver designed and realized for the Basic Element for SKA Training (BEST-2) European Commission – SKA Design Study (EC-SKADS) demonstrator [*Perini et al.*, 2009]. It provides RF band filtering of 16 MHz around 408 MHz, the conversion to an intermediate frequency at 30 MHz, and the necessary analog amplification in order to feed the ADC board. Moreover, it allows to control the amplitude level with 0.5 dB accuracy using digital step attenuator in the RF receiver chain. The digital back end for the MAD experiment has been developed using the Reconfigurable Open Architecture Computing Hardware (ROACH-1) Collaboration for Astronomy Signal Processing and Electronics Research (CASPER) (https://casper.berkeley.edu/) board, which is a XILINX VIRTEX-5 Field Programmable Gate Array (FPGA) integrated on a mainboard populated with many peripherals. The aim of the digital back end is to digitize the IF analog signals and to produce the array beam in both polarizations; furthermore, the correlation products are calculated for the array calibration [*Pupillo et al.*, 2015].

While the MAD back end works with a small number of inputs and processes a narrow bandwidth (20 MHz), SAD needs a scalable high-performance and wideband back end. These objectives are accomplished by the

Table 1. General Specification of the Architecture of the Italian Demonstrators Compared To LFAA Element of SKA1-LOW and to AAVS1[a]

	MAD	SAD	AAVS1	LFAA of SKA1-LOW
Frequency band	400–416 MHz	270–375 MHz phase 1; 270–420 MHz phase 2	50–350 MHz (with a possible extension up to 650 MHz)	50–350 MHz
Array				
Antenna	Vivaldi 2.0	Vivaldi 3.1	SKALA 2.0	SKALA 2.0
Number of elements	9	128	400	2^{17} (131,072)
Number of stations	-	1BIG: one station with 128 antennas (max 64 m diameter) or 8SMALL: 8 stations with 16 antennas each (max 15 m diameter)	one station with 256 antennas (35 m diameter) and three stations with 48 antennas	500 stations (35 m diameter)
Configuration	Regularly spaced in a rhomboidal configuration	Randomly spaced in a flexible configuration	Randomly spaced in a flexible configuration	Randomly spaced
Maximum baseline	4 m	250 m	180 m	65 km
Front end	LNA + OTX (without preamp)	LNA + intermediate RF gain block + OTX (with preamp)	LNA + OTX (with preamp)	LNA + OTX (with preamp)
Signal transportation	RFoF (one optical fiber for each polarization)	RFoF (one optical fiber for both polarizations)	RFoF (one optical fiber for both polarizations)	RFoF
RF receiver	Amplification, equalization, filtering, and frequency down conversion	Amplification, equalization, and filtering	Amplification, equalization, and filtering	Amplification, equalization, and filtering
Digitization	12 bits, 40 MSPS[b]	8 bits, 1 GSPS[b] (TBC)	8 bits, 800 MSPS	8 bits, 800 MSPS
Back end for frequency channelization, calibration, and station beam forming	ROACH-1	Tile Processing Module	Tile Processing Module	Tile Processing Module

[a]For a complete description of the SKA Log-periodic Antenna (SKALA) 2.0 see *de Lera Acedo et al.* [2015].
[b]MSPS = Mega-Samples per second; GSPS = Giga-Samples per second; TBC = To be confirmed.

Tile Processing Module (TPM). This is a rack-mounted unit that forms one coherent beam from a group (tile) of 16 dual polarizations antennas (32-signal chains). The TPM is composed of two subsystems: the Preanalog to Digital Unit (ADU) and the Analog to Digital Unit (preADU) boards. The purposes of the analog receiver subsystem PreADU are the following: (i) convert back the optical signals to electrical, (ii) amplify and equalize the antenna RF signals, (iii) band pass the signals in order to avoid Nyquist aliasing, and finally (iv) provide the optimal analog signal level to the ADC to maximize the dynamic range of the whole back end.

The ADU board has two powerful Xilinx Kintex UltraScale XCU40 (20 nm technology) FPGAs that allow to perform digital processing on up to 500 MHz of bandwidth. The calibration procedure and the ADU management is carried out by a dedicated workstation named local monitor and control that provides amplitude equalization coefficients and phase calibration coefficients to be loaded into the ADUs.

3. Radio Frequency Monitoring at the Two Sites

During the design phase of the two demonstrators, intensive radio frequency monitoring campaigns were conducted at the sites. These were mainly aimed to the following: (i) verify the statistical spectral occupancy below 500 MHz to identify the portion of the radio spectrum least polluted by other terrestrial services and (ii) characterize the power levels of the strongest signals

Figure 3. (left column) Antenna mechanics and (right column) zoom for the electronics integration. (top row) Vivaldi 2.0 for MAD; (bottom row) Vivaldi 3.1 for SAD.

(broadcast FM radio and services radio links) to accurately design the receiver chain especially in terms of RF filters.

For the two sites, the monitoring has been performed using similar receiving RF chains basically composed by log-periodic antenna, coaxial cable, and portable spectrum analyzer. Data were collected for both the horizontal and the vertical polarizations. For each of the two polarizations, we produced max hold spectra over 360 deg by pointing the antenna in six different angular positions evenly spaced by 60°. For these

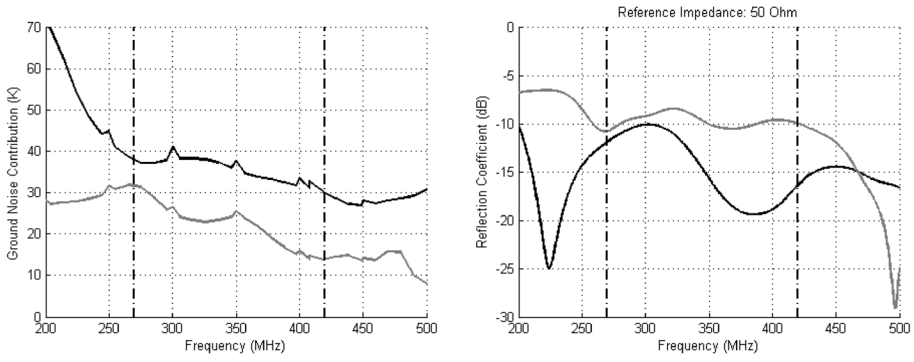

Figure 4. (a) Ground noise contribution for Vivaldi 2.0 (black) and Vivaldi 3.1 (gray). (b) Reflection coefficient for Vivaldi 2.0 (black) and Vivaldi 3.1 (gray). The vertical lines highlight the final SAD frequency band: 270–420 MHz.

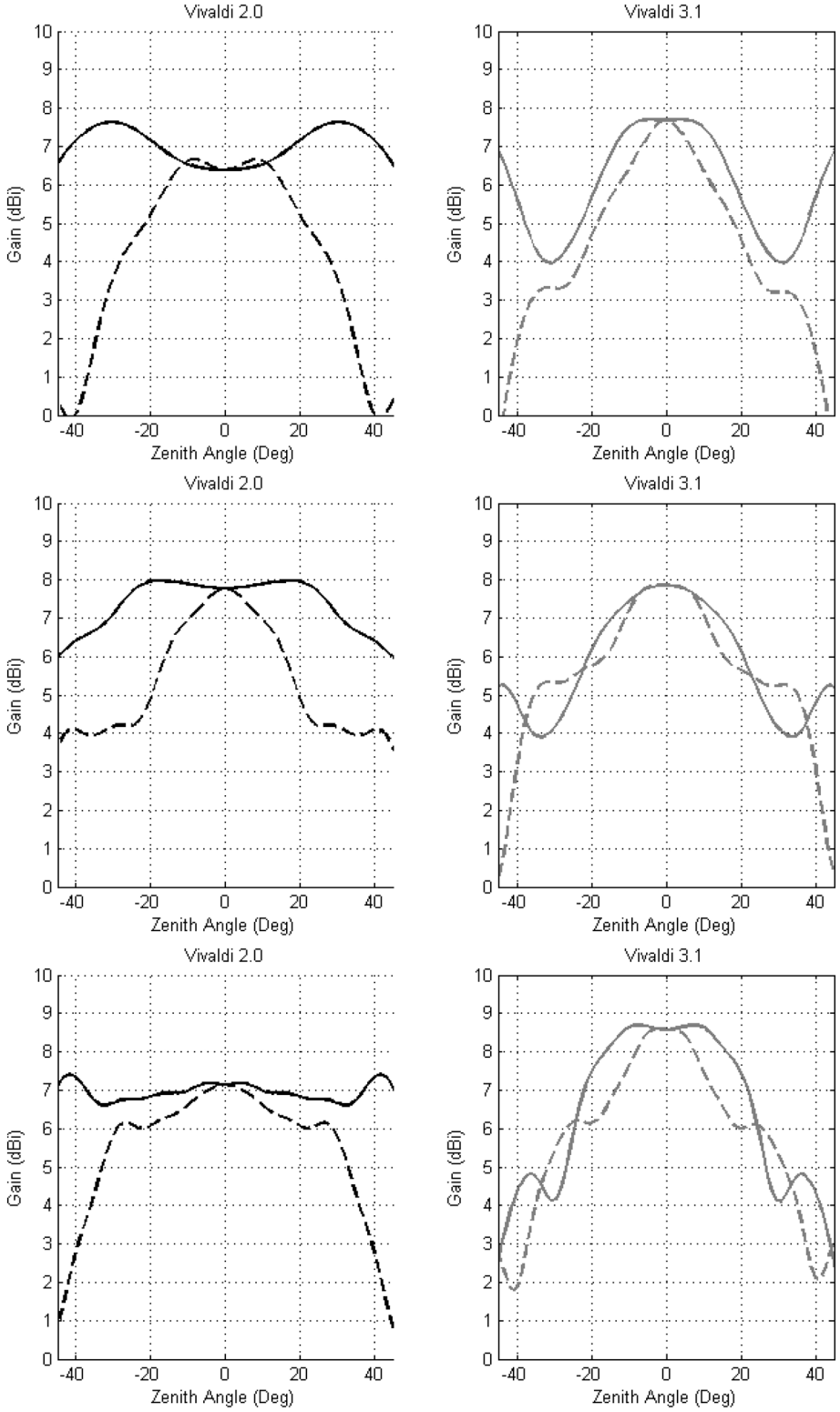

Figure 5. Radiation patterns of the (left column) Vivaldi 2.0 and (right column) Vivaldi 3.1: *H* plane (solid line) and *E* plane (dashed line). (top, middle, and bottom rows) Frequencies: 250, 350, and 450 MHz.

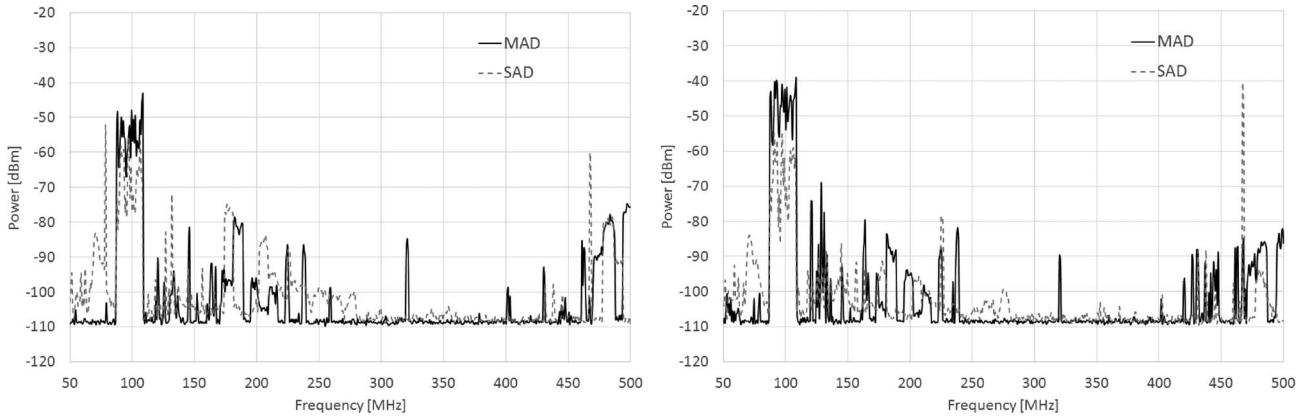

Figure 6. Spectra in the frequency band 50–500 MHz collected at the Medicina station (black continuous lines) and at the SRT site (gray dashed lines): (left) horizontal and (right) vertical polarization. Each data set has been normalized for the different antenna gains and the different losses of the coaxial cables of the two systems.

measurements, the spectrum analyzer resolution bandwidth and video bandwidth were both set to 10 kHz, the attenuation factor was set to 0 dB, and finally the sweep time was around 10 s.

Figure 6 shows the spectra for both linear polarizations on the frequency band 50–500 MHz collected at the Medicina station and at the SRT site. For what concerns the strongly contaminated spectral regions around 100 MHz (FM radio broadcast) and in between 450 and 500 MHz, the RF situation at the SRT site is quite similar to that measured at the Medicina station. Nevertheless, it is worth to mention that in general the intensity of the artificial signals at the SRT site is significantly lower than that at the Medicina station, mainly in the FM frequency range. In between 50–80 MHz the power level seems to be slightly higher at the SRT site. The Medicina spectra show higher signals around 125 MHz, 240 MHz, 330 MHz, and in between 400 and 450 MHz. Finally, at the SRT site we observe a few strong narrow band signals above 425 MHz for the vertical polarization.

In conclusion, as already said, for MAD the natural choice was to use the protected frequency band around 408 MHz where several infrastructures were already available. Whereas, in SAD, the RFI scenario is such that no radio frequency filter is required in front of the LNA and the 270–420 MHz spectral window was selected as the cleaner band for astronomical observations.

4. UAV Source for the Array Calibration

The hexacopter developed in the framework of MAD and SAD is a custom product based on a GPS-board Mikrokopter, which automatically follows waypoints (see Figure 7). The UAV is equipped with a continuous wave synthesizer connected to a transmitting antenna. The frequency range of the system is from 5 to 4400 MHz. The UAV position is measured every second with differential GNSS (Global Navigation Satellite System), allowing a spatial accuracy of few centimeters. An inertial measurement unit, installed on board of the hexacopter, measures the three orientation angles. All the position and orientation data are used during the postprocessing analysis for determining the actual electric field illuminating the antenna under test (AUT).

Figure 7. The UAV taking off at the Medicina Array Demonstrator.

The UAV system allows to calibrate and measure in real operative conditions

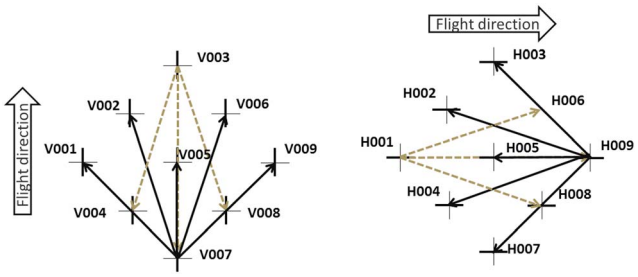

Figure 8. Scheme of the baseline subsets selected for the array calibration in (left) *Y* and (right) *X* polarization.

the far-field antenna/array patterns as well as to check the element integrity and measure both orientation and position of the antenna under test. The usage of the UAV for the instrumental calibration of an aperture array can play a significant role to obtain a correctly shaped and oriented array beam.

The instrumental calibration is necessary to remove the systematic effects due to the differences in each receiving chain (due, for instance, to the signal path lengths, to the drifts in the electronic gains, and to the coupling among the antennas). This process is done by appropriately weighting in amplitude and phase the signal received by each element. In order to evaluate such a complex coefficients, the UAV systems proved to be a very promising solution for injecting a known signal. As a matter of fact, for the artificial sources the reference signal is stable and tunable. For example, by increasing the transmitted power level of the reference antenna, it is possible to reach the required signal-to-noise ratio (SNR). On the other hand, the UAVs are limited in the maximum height of the flight, which in turn sets the maximum size and/or the maximum frequency of the array under test in far-field conditions.

Unlike the instrumental calibration, that is occasionally performed, for example, at the initial stage and in case of major hardware modifications, a radio astronomical aperture array needs to be regularly and frequently (around every tens of second or minutes) calibrated during the observations by means of classical astronomical calibration techniques. The latter procedures aim to measure and to remove the undesired contributions from the sky (e.g., bright sources in the sidelobes, galactic foreground, and unresolved sources) and from the atmosphere (especially the ionosphere at low frequency). Such an astronomical calibration is not addressed in this paper.

5. Insights in the MAD Calibration

5.1. Instrumental Calibration

MAD allowed us to test a number of calibration strategies using the UAV as a reference source transmitting a 408 MHz radio frequency signal. Different calibration methods were exploited in the second and third test MAD campaigns, hereafter referred to MAD-2 (October 2013) and MAD-3 (May 2014), respectively. In particular, the MAD-2 amplitude calibration coefficients were calculated in order to minimize the differences between the observed and the expected (by electromagnetic simulations) power received from each antenna when the source was at the zenith. On the other hand, for MAD-3 we chose to digitally equalize the signal power for all antennas, again with the UAV at the zenith. From the phase point of view, MAD-2 exploited a fringe-fitting method, while for MAD-3 a phase-snapshot technique was used [*Pupillo et al.*, 2015]. Each calibration technique requires a proper flight strategy: linear scans for fringe-fitting and still flights for phase snapshot and amplitude calibration.

The calibration methods exploited in MAD-3 had some advantages with respect to those utilized in the MAD-2 campaign. In particular, the amplitudes calibration in MAD-3 is model-independent and the phases are calibrated for the specific direction in which the array beam forms.

The MAD digital back end included not only a beam former but also a correlator for the array calibration. The digital correlator calculated the correlation products of the signals $V(t)$ received from any couple of array elements (ith and jth) forming an interferometer baseline, as: $R_{ij} = \left\langle V_i(t) V_j^*(t) \right\rangle$ with $i \neq j$. In principle, an array of N antennas forms $N(N-1)/2$ independent baselines. Even if MAD yields 36 independent baselines, in MAD-2 and, to some extent, also in MAD-3 we preferred to use a digital back-end firmware programmed to produce cross correlations for a proper subset of eight baselines for each polarization (Figure 8), in order to reduce the data rate and minimize the risk of data loss between the digital back end and the storage server. The MAD principal antenna polarizations *X* and *Y* were oriented along the directions E-W and N-S, respectively.

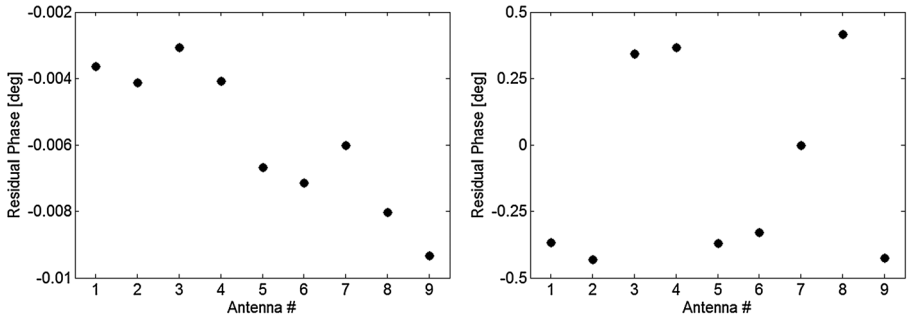

Figure 9. Mean value of the differences between the phases calculated by standard method and LSM for UAV flights at the angles (left) $\theta = 0°$ and (right) $\theta = 45°$ for each element of the array with respect to the V007 reference antenna.

The baseline subset selection criterion aimed to maximize the fringe frequency in the direction of the UAV trajectory, so as to increase the calibration accuracy when using the fringe-fitting method. Each relative phase obtained from the complex crosscorrelations is the sum of two main terms: the intrinsic instrumental phase and the phase associated to the delay due to the different geometric paths from the source to the various array elements. The actual UAV position along the trajectory is obtained via differential GNSS measurements; thus, it is possible to extract the instrumental phase term from the measured phase of the cross-correlation terms with high accuracy. Then, the phase calibration coefficients, calculated from the instrumental phases, are loaded in the digital back end together with the calibration amplitude coefficients estimated through the autocorrelations.

Fringe patterns were produced by means of UAV rectilinear flights across the field of view (FoV). After the calibration the alignment of the main fringe maxima at zenith for all the acquired baselines demonstrates an accurate array phase calibration in that direction [*Pupillo et al.*, 2015].

In the last part of the MAD-3 campaign, a new firmware was installed and tested on the digital back end operating in parallel with the old one. The upgraded back end was able to calculate also the full-array correlation matrix (ACM) that allowed us to produce 36 independent cross correlations instead of the eight correlation products generated by the previous firmware version.

The use of the ACM in the phase calibration therefore led to an overdetermined system of equations (36 equations for eight unknowns) that could be exploited to improve the accuracy in the phase solutions by a statistical approach. In particular, we optimized the phase solutions by means of the least squares method (LSM). The advantage of such an overconstrained estimator is to increase the accuracy and robustness of the phase determination when the SNR is low.

The phase solutions calculated using the minimal set of eight cross correlations (old firmware) and those estimated by the LSM method (new firmware) were compared. Figure 9 shows the differences between the phases computed with these two approaches with the UAV positioned at zenith (left) and at an angle $\theta = 45°$ (right). By comparing the two plots of Figure 9, it turns out that the relative lower power level (and consequently a lower SNR) received by the AUT when the UAV is at $\theta = 45°$ with respect to that received from the zenith direction, increases the differences between the solutions obtained by the two methods. However, the difference values remains negligible in both cases.

The results of these measurements demonstrated that using an extremely strong calibration source, as the UAV in our tests, the advantages of the LSM for the phase calibration are negligible. However, the benefits of overconstrained estimator in terms of accuracy could be significant in case of low-power transmission.

There are many errors that affect, both in phase and amplitude, the cross correlations acquired by an interferometer. These errors can be divided into two main groups: antenna-based errors that are related to individual antennas and are factorable to each array element in the measurement equation and baseline-based errors that are related to single baselines. It is known that proper combinations of phases or amplitudes produce quantities in which all the antenna-based errors (due to atmosphere, cable lengths, electronics, etc.) cancel out. These quantities, called closures, are widely used in the self-calibration procedures [*Pearson and Readhead*, 1984] and they can also be useful to check for the correlator errors and other baseline-based errors. Each phase

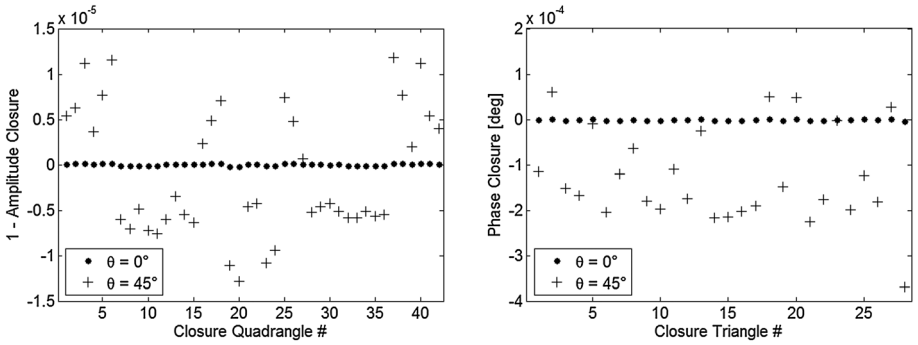

Figure 10. (left) The quantity $1 - A_{klmn}$ for each closure quadrangle and (right) phase closure for every independent closure triangle both calculated from MAD-3 data at the angles $\theta = 0°$ (dots) and $\theta = 45°$ (crosses). The *y* axis scale is 10^{-5} for the left plot and 10^{-4}° for the right plot.

closure Φ_{ijk} is calculated from a proper set of three baselines forming a triangle (closure triangle) as $\Phi_{ijk} = \varphi_{ij} + \varphi_{jk} + \varphi_{ki}$ in which φ_{ij} is the phase of the cross-correlation R_{ij}. Similarly, every closure amplitude A_{klmn} is derived from an appropriate set of four baselines forming a close quadrangle (closure quadrangle) as $A_{klmn} = \frac{|R_{kl}||R_{mn}|}{|R_{km}||R_{ln}|}$ that is independent of the antenna-based errors [*Wilson et al.*, 2009].

It is important to verify whether the UAV is a suitable source to evaluate the baseline-based errors via the closures analysis. For this purpose, phase and amplitude closures were derived from the ACM acquired in the MAD-3 campaign. Figure 10 displays the values ($1 - A_{klmn}$) (left) and the phase closures (right), both calculated for the UAV flights at zenith angle 0° (dots) and 45° (crosses).

For both angles, the measured phase and amplitude closures were very close to values 0 and 1, respectively. Since the closure quantities are independent of antenna-based errors, these are the values expected for a symmetric or a point-like (unresolved) source when the baseline-based errors are negligible.

This result demonstrates that the UAV can be an effective tool not only for the array calibration and characterization over the entire FoV but also to check the system integrity from the baseline-based errors point of view.

5.2. Analysis of the Calibration Residuals

As reported in section 5.1, the phase calibration during MAD-3 was performed at 408 MHz with the UAV close to zenith. In particular, the zenith position is set as a goal for the navigation system. Actually, the real UAV position can generally be 2 or 3 m far from such a goal. Nevertheless, such a discrepancy is compensated for by using the more accurate position information measured by the differential GNSS system.

A result example of this procedure is shown in Figure 11. Figure 11 (top) represents the real position of the UAV measured with the GNSS system in the horizontal plane (the flying height is about 100 m). On the other hand, Figure 11 (bottom) reports the measured differential phase shift (phase of the cross-correlation coefficient) for the baseline V003-V007 (black line) defined in Figure 8. According to the procedure in [*Pupillo et al.*, 2015], the position data were used to compute the difference of geometric delay between the two UAV antenna paths. The corresponding phase contribution was then subtracted from the measured differential phase shift. The residual phase error is reported in Figure 11 (bottom) with gray line, showing that the effect of the UAV displacement has been compensated.

The residual phase error in Figure 11 (bottom) has been averaged (256 samples) to remove the phase noise and sampled at 1 Hz in order to avoid any interpolation error from the GNSS data. The resulting curve is shown in Figure 12 with the solid line and circles. The peak-to-peak error is about 2.5° whereas the computed standard deviation σ_ϕ is 0.55°. The black dots represent the boundary $\pm\sigma_\phi$ from the average value.

The explanation of this residual phase error can be found considering the standard deviation of the GNSS position data. As matter of fact, since the baseline V003-V007 is oriented along the *y* axis, its differential phase is only proportional to the *y* component of the UAV displacement (black curve in Figure 11 (top)). In this case,

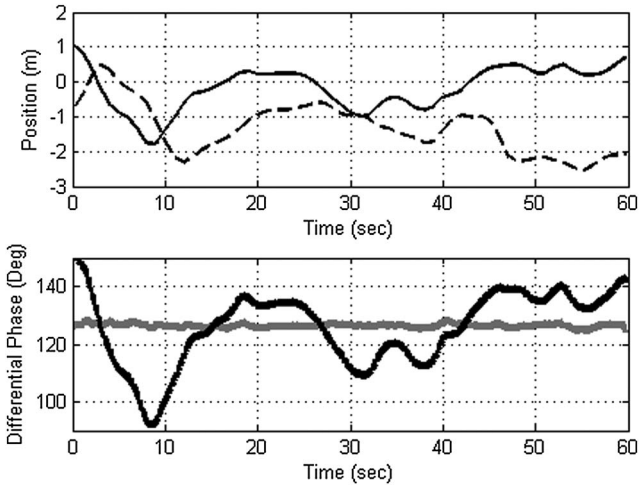

Figure 11. (top) Position of the UAV measured with the differential GNSS system: *x* coordinate (dashed) and *y* coordinate (continuous). (bottom) Measured differential phase shift for baseline V003-V007 (black) and residual phase after correction (gray).

the phase contribution due to small UAV displacements around zenith can be evaluated using the following relationship (far-field approximation):

$$\Delta\phi = \frac{2\pi}{\phi} L_b \frac{y}{z}$$

where L_b is the distance between the two antennas, λ is the wavelength, y and z are the UAV coordinates with respect to the array center. Hence, the relationship between the standard deviation of the residual phase error σ_ϕ and the standard deviation of the GNSS data along the y direction σ_y is

$$\sigma_\phi \cong \frac{2\pi}{\lambda} L_b \frac{\sigma_y}{z}$$

The value of σ_y is obtained as output of the GNSS data elaboration procedure. For the stationary flight shown in Figure 11, a value of about 2 cm has been obtained. This value leads to a σ_ϕ of about 0.4 (L_b is 4.24 m). The corresponding gray error bar in Figure 12 demonstrates that the estimated σ_ϕ is consistent with the measured results, confirming that the GNSS precision is the most important contribution to the residual phase error.

Another capability of the UAV-based calibration system consists in the measurement of the difference between the phase patterns of the two antennas of each baseline. Even if the antennas are identical, each of them has a specific position inside the array. Therefore, they show different phase patterns due to the mutual coupling among the antennas and different angles toward the UAV transmitter. These parameters can be directly obtained from the measured cross-correlation coefficients [see *Pupillo et al.*, 2015] during a rectilinear flight of the UAV over the array. In particular, the same compensation procedure discussed above is adopted here, which consists in subtracting the geometric phase delay from the phase of the measured cross-correlation coefficients. In this case, since the UAV moves in the overall FoV of the antennas, the main contribution to the residual phase corresponds to the differential phase pattern. Figure 13 shows both the measured (solid line) and simulated (dashed line) *E* plane differential phase patterns of the eight MAD baselines normalized at zenith. The overall agreement is good. The observable discrepancies are mainly related to the position and orientation accuracy of the UAV, to the simulation accuracy, and to the real placement of the antennas on ground. The knowledge of these phase differences will lead to a more efficient beam forming of the overall system.

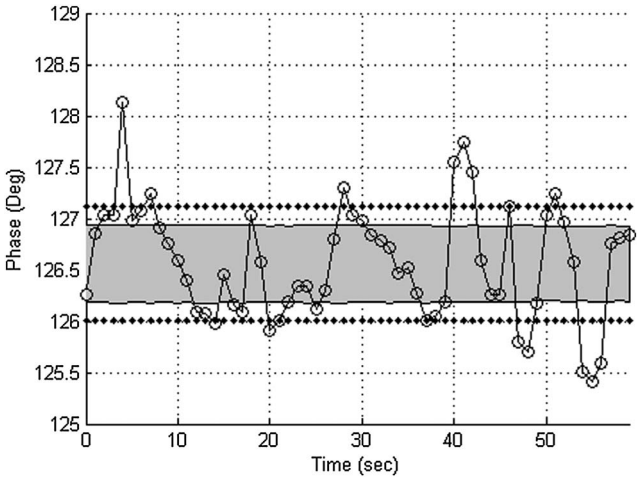

Figure 12. Residual phase error after compensation of the UAV displacement (solid line with circle), measured and estimated by GNSS standard deviation (black dots and gray area, respectively).

6. Numerical Analysis of SAD

The size of the SAD stations is similar to that planned for the future LFAA of SKA1-LOW, and therefore, SAD represents a more significant case for verifying the UAV potentialities for the instrumental calibration of an aperture array. In particular, in this section we evaluates how much the mutual coupling impacts on the antenna embedded patterns.

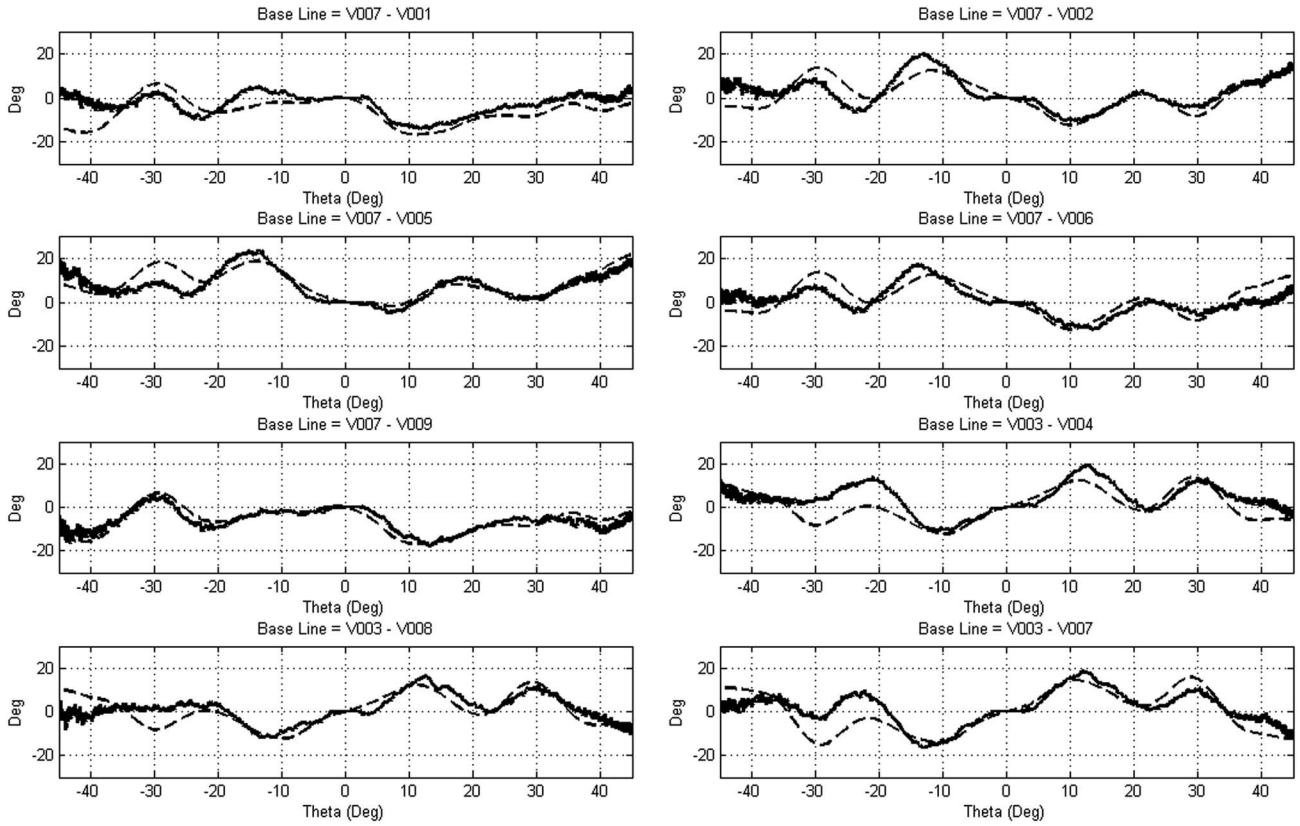

Figure 13. *E* plane measured (solid) and simulated (dashed) differential phase patterns for the eight baselines of MAD.

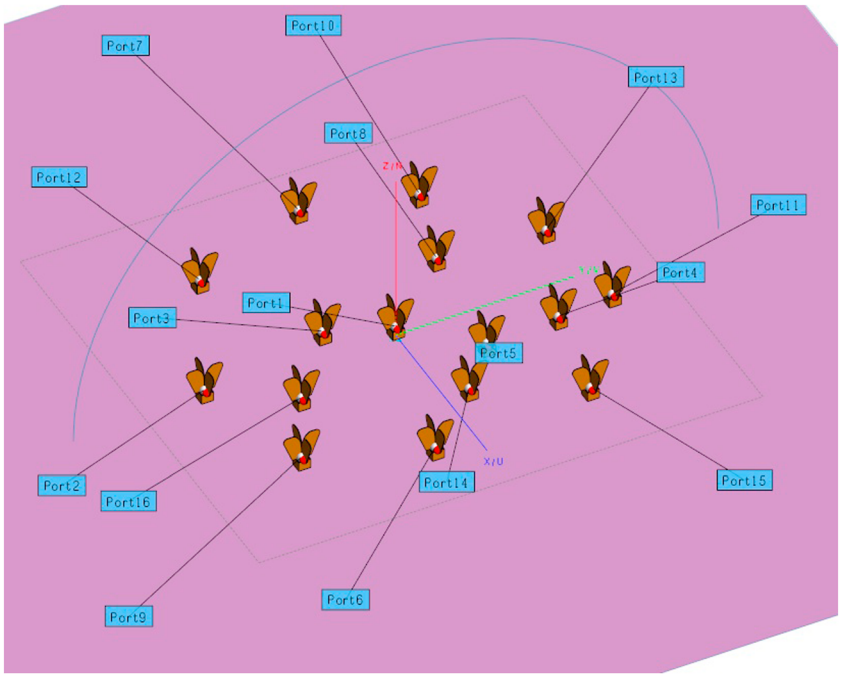

Figure 14. Geometry of a station of SAD. The array is composed by 16 antennas, with antenna 1 centered in the origin and antenna 9 at the maximum distance from the origin (7.45 m, coordinates: $x = 4.6$ m and $y = -5.9$ m). The circular line indicates the *H* plane where the far-field patterns are computed.

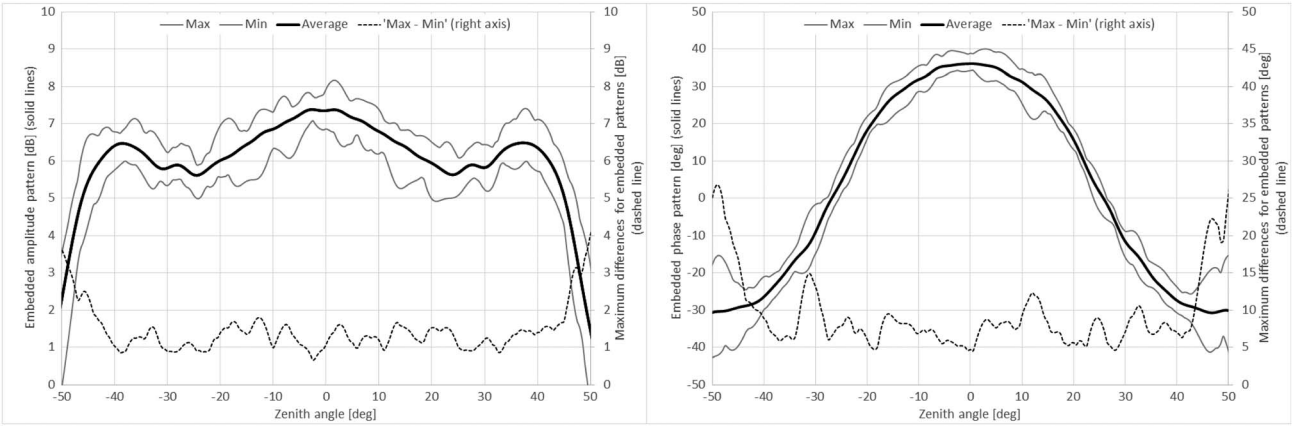

Figure 15. Average, maximum, minimum, and maximum differences for the embedded patterns of the 16 antennas in the *H* plane for (left) amplitude and (right) phase.

In order to keep the computation time at a reasonable level, we have considered a station of SAD composed by 16 antennas (configuration 8SMALL) with a random spatial distribution (see Figure 14). As a first case, we simulated a diameter station of 15 m, which represents the initial size of the 8SMALL configuration. In this case, the antenna spatial density is quite low with respect to that planned for the LFAA element of SKA1-LOW. Therefore, this geometry gives an underestimation of the mutual coupling effects with respect to that in a denser antenna distribution. The maximum and minimum distances among the antennas of our model are 14.5 and 2.1 m, respectively, with an average of 7.9 m. However, thanks to the array reconfigurability, it will be possible to compact the antennas in a denser configuration.

All the antennas are aligned in the same direction and lay on an infinite ground plane (placed at $z = 0$) with relative electrical permittivity equal to 8 and 0.35 of dielectric loss tangent. The cavity of the antenna lies exactly on the ground plane without any gap of air, whereas the antenna probes are 39 cm above the ground.

The analysis was performed by using the full-wave electromagnetic simulator FEKO version 7.0 based on the method of moment (https://www.feko.info/). The frequency chosen for the analysis is 350 MHz.

The embedded pattern of each antenna is computed by taking into account the mutual coupling with the other antennas of the array. Such an effect perturbs both amplitude and phase patterns with respect to

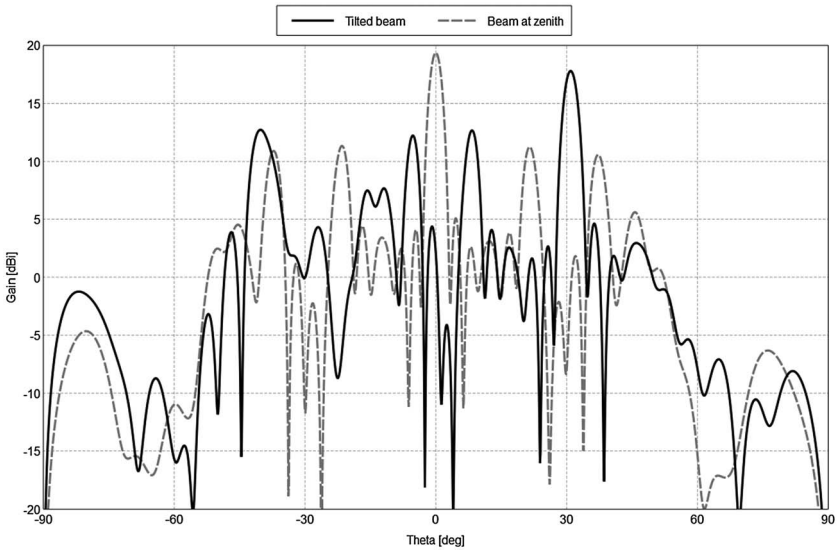

Figure 16. Array patterns for a station of SAD in the *H* plane with two different sets of phase coefficients for zenith and tilted pointing.

the stand-alone case. The average of the embedded patterns together with their maximum and minimum values is shown, for the *H* plane, in Figure 15. All the embedded patterns are therefore included between the two gray curves. In the FoV of the element, the amplitude and phase maximum differences among the patterns are quite significant: up to 2 dB for the amplitude and 15° for the phase, as shown in the dashed curves. Further analysis will give more accurate indications on how much these deviations affect the array pattern and the possible benefits to take them into account during the array calibration.

Finally, the array pattern has been computed by applying the geometrical delays to each antenna to form the beam in two different directions: at zenith and tilted at around 30° in the *H* plane. The array patterns at 350 MHz are plotted in Figure 16 where it is evident, for the tilted beam, the reduced power level of the main beam and the increase of the sidelobe levels. However, due to the random spatial distribution of the antennas, no grating lobes appear. The phase coefficients have been evaluated only from the antenna positions without taking into account the variations on the embedded patterns of each antenna due to the electromagnetic coupling. These secondary effects will be included in a future step of the analysis.

7. Discussion

MAD gave us the opportunity to acquire real experience with a small aperture array. However, it was a temporary instrument expected to operate in good environment conditions and for short duration experiments. On the other hand, SAD posed harder challenges due to its larger size and especially to its permanent installation, which required mechanic and electronic solutions to survive to the more hostile environmental conditions expected in a quite long period. Two examples of the specific designs adopted in SAD are the mesh wings for the Vivaldi 3.1 antennas and the waterproof protection of the boxes containing the electronics. Moreover, the SAD design was further complicated by the flexibility in the architecture to allow for different array reconfigurations. Therefore, we selected robust and manageable cables to avoid damages during the deployment and the operation phases, and hybrid connectors quick to plug.

A peculiar feature of the two demonstrators is related to the decision to avoid metallic cables between the antennas and the receivers, limiting the impact of the cables on the antenna radiation pattern. Therefore, we implemented the RFoF technology for the signal transportation. As far as the front ends bias is concerned, MAD used batteries inside the antennas. However, this solution was adequate for short test durations (few hours). Consequently, in view of SAD, which aims to perform continuous operation, we are investing substantial resources in the power over fiber technique.

From the back end and calibration point of view, MAD allowed us to test several operational strategies and to achieve some important conclusions in perspective to SAD. The capability of the back end firmware to be highly reconfigurable, as successfully tested in the MAD-3 campaign, shall be necessary for SAD due to its flexible configuration and hierarchical structure. The MAD experience demonstrated also that a proper minimal subset of cross correlations is sufficient to calibrate the system when the UAV is used as a very strong and stable reference source. However in SAD, where also astronomical sources will be used as calibrators, the full ACM could be essential for the station/array calibration.

The measurement campaign of MAD-3 demonstrated also a significant sensitivity of the antenna pattern with respect to the antenna-ground distance. Such a distance was not constant owing to a noncontrolled planarity of the soil ground under the array. This drawback is not particularly serious in SAD since the Vivaldi 3.1 design is less sensitive to the ground. Moreover, the antenna will be placed at a constant height owing to its support structure. However, further design work could be performed in order to minimize the soil effect to a greater extent with a consequent reduction of the corresponding ripple of the antenna parameters versus frequency as well. A further remark is in the antenna spatial precision during the deployment phase (few millimeters for MAD), which was significantly difficult to reach. Therefore, in SAD, such a requirement will be relaxed, and we will rely on the photogrammetry camera on board of the hexacopter for accurately measuring the positions of the antennas.

As described in the paper, the array calibration with artificial source is based on an accurate measurement of the source relative position with respect to the array. The position data are combined with the RF data recorded with the back end in order to compute all the array parameters (differential phase shifts, patterns, etc.). The MAD experience showed that the time synchronization between these two data sets is not trivial: position

and RF data are time stamped with the GNSS clock and the Medicina station clock, respectively. As a consequence, the synchronization between the two clocks should be properly verified during the measurements.

From the operative point-of-view, the MAD experience also demonstrated that besides the required setup time and resources, the overall calibration process still requires a certain number of people to control the UAV, setup the RF source, elaborate the position and orientation data, configure the back end, and combine all the data. A significant amount of effort is being invested in order to reduce the number of involved people and the required time for the overall process. Especially for a possible use in the SKA project, a more automatic control of the UAV would be extremely important.

8. Conclusions

In the last years, radio astronomy has been pushing toward the lowest frequencies of the radio spectrum available at ground level. Fundamental questions in astrophysics can be addressed in this frequency range. The low-frequency aperture array systems proved to be excellent instruments for this purpose. In order to increase knowledge in this area, two national technological demonstrators, MAD and SAD, were designed for implementing LFAA systems. The small MAD was used for testing several components both hardware and software and especially for verifying the instrumental calibration of the array by using an artificial source mounted in an aerial vehicle. This turned out to be a reliable and accurate tool for proper evaluating the phase and amplitude coefficients. More significant results are expected from SAD whose architecture and size of the stations are quite similar to those of SKA1-LOW.

Acknowledgments
The Sardinia Array Demonstrator is funded by the Sardinian Regional Government, L.R. 7 Agosto 2007, N.7: "Promozione della Ricerca Scientifica e dell'innovazione Tecnologica in Sardegna," Progetti di ricerca fondamentale o di base annualità 2012; CRP-60151, PI M. Murgia. Further financial resources for SAD come from INAF through two TECNO INAF projects entitled "Digital Platform development for back end design of new generation SKA Aperture Arrays" (PI F. Schillirò) and "Advanced calibration techniques for next generation low-frequency radio astronomical arrays" (PI P. Bolli) funded in 2012 and 2014, respectively. The authors would like to thank F. Govoni, F. Gaudiomonte, R. Ambrosini, C. Bortolotti, and M. Roma who performed the RF environment investigations at the two sites and then analyzed the data. Interested people can request the data published in this article by contacting P. Bolli: pbolli@arcetri.inaf.it.

References

Bolli, P., et al. (2015), Sardinia Array Demonstrator: Instrument overview and status, *Int. Conf. Electromagn. Adv. Appl.*, 682–685, doi:10.1109/ICEAA.2015.7297200.

Carozzi, T. D. (2015), Intrinsic cross-polarization ratio (IXR) for antenna arrays and improving polarimetry via polarization diversity, *Int. Conf. Electromagn. Adv. Appl.*, 630–633, doi:10.1109/ICEAA.2015.7297193.

Chang, C., C. Monstein, A. Refregier, A. Amara, A. Glauser, and S. Casura (2015), Beam calibration of radio telescopes with drones, *Publ. Astron. Soc. Pac.*, *127*(957), 1131–1143, doi:10.1086/683467.

de Lera Acedo, E., N. Razavi-Ghods, N. Troop, N. Drought, and A. J. Faulkner (2015), SKALA, a log-periodic array antenna for the SKA-low instrument: Design, simulations, tests and system considerations, *Exp. Astron.*, *39*(3), 567–594, doi:10.1007/s10686-015-9439-0.

Dewdney, P. (2015), SKA1 system baseline v2 description. [Available at https://www.skatelescope.org/key-documents/.]

Fiorelli, B., M. Arts, G. Virone, E. de Lera Acedo, and W. A. van Cappellen (2013), Polarization analysis and evaluation for radio astronomy aperture array antennas, 7th European Conference on Antennas and Propagation, 461–465.

Kraus, J. D. (1984), *Radio Astronomy*, Cygnus-Quasar Books, Powell, Ohio.

Monari, J., et al. (2013), Aperture array for low frequency: The Vivaldi solution, *Int. Conf. Electromagn. Adv. Appl.*, 66–69, doi:10.1109/ICEAA.2013.6632191.

Murgia, M., et al. (2014), Sardinia aperture Array Demonstrator, *Proc. SPIE*, *9145*, doi:10.1117/12.2055793.

Pearson, T. J., and A. C. S. Readhead (1984), Image formation by self-calibration in radio astronomy, *Annu. Rev. Astron. Astrophys*, *22*, 97–130.

Perini, F., G. Bianchi, M. Schiaffino, and J. Monari (2009), BEST receiver experience: general architecture, design and integration, Proceedings of Widefield Science and Technology for the SKA, SKADS Conference, Chateau de Limelette, Belgium.

Perini, F., S. Rusticelli, M. Murgia, J. Monari, M. Agnoletto, G. Viola, and G. Tartarini (2015), Power over Fibre systems for the Italian SKA-LOW demonstrators, Fotonica AEIT Italian Conference on Photonics Technologies, 1–4, doi: 10.1049/cp.2015.0169.

Pupillo, G., et al. (2015), Medicina array demonstrator: Calibration and radiation pattern characterization using a UAV-mounted radio-frequency source, *Exp. Astron.*, *39*(2), 405–421, doi:10.1007/s10686-015-9456-z.

Virone, G., A. M. Lingua, M. Piras, A. Cina, F. Perini, J. Monari, F. Paonessa, O. A. Peverini, G. Addamo, and R. Tascone (2014), Antenna pattern verification system based on a micro unmanned aerial vehicle (UAV), *IEEE Antenn. Wireless Propag. Lett.*, *13*, 169–172, doi:10.1109/LAWP.2014.2298250.

Wilson, T. L., K. Rohlfs, and S. Huttemeister (2009), *Tools of Radio Astronomy*, pp. 220–221, 5th ed., Springer, A&A Library, Berlin, doi:10.1007/978-3-540-85122-6.